

# Mechanoregulatory Cholesterol Oxidase-Functionalized Nanoscale Metal–Organic Framework Stimulates Pyroptosis and Reinvigorates T Cells

Wenyao Zhen, Taokun Luo, Zitong Wang, Xiaomin Jiang, Eric Yuan, Ralph R. Weichselbaum, and Wenbin Lin\*

Cancer cells alter mechanical tension in their cell membranes. New interventions to regulate cell membrane tension present a potential strategy for cancer therapy. Herein, the increase of cell membrane tension by cholesterol oxidase (COD) via cholesterol depletion *in vitro* and the design of a COD-functionalized nanoscale metal–organic framework, Hf-TBP/COD, for cholesterol depletion and mechanoregulation of tumors *in vivo*, are reported. COD is found to deplete cholesterol and disrupt the mechanical properties of lipid bilayers, leading to decreased cell proliferation, migration, and tolerance to oxidative stress. Hf-TBP/COD increases mechanical tension of plasma membranes and osmotic fragility of cancer cells, which induces influx of calcium ions, inhibits cell migration, increases rupturing propensity for effective caspase-1 mediated pyroptosis, and decreases tolerance to oxidative stress. In the tumor microenvironment, Hf-TBP/COD downregulates multiple immunosuppressive checkpoints to reinvigorate T cells and enhance T cell infiltration. Compared to Hf-TBP, Hf-TBP/COD improves anti-tumor immune response and tumor growth inhibition from 54.3% and 79.8% to 91.7% and 95% in a subcutaneous triple-negative breast cancer model and a colon cancer model, respectively.

bilayers, determines cell morphologies, controls adhesion, migration, and division of cells,<sup>[2]</sup> and influences mechanosensitive ion channels<sup>[3]</sup> and material transport in the cytoplasm.<sup>[4]</sup> Under normal physiological conditions, cell membranes are resistant to mechanical tensions of up to  $10^{-2}$  N m<sup>-1</sup>.<sup>[5]</sup> When faced with external stress, cells can create membrane invaginations/blebs, regulate cytoskeletal–membrane connections passively, and adjust mechanosensitive channels and membrane trafficking actively to resist lysis.<sup>[6]</sup> However, cells physically rupture when the strain on membrane lipids exceeds a threshold. Even though membrane pores below a critical size can rapidly reseal, they make the membrane unstable. As cancer cells are known to have altered mechanical tension in their cell membranes, new interventions to regulate cell membrane tension may present a novel approach to kill cancer cells.


Cholesterol is a crucial lipid molecule for regulating the fluidity and permeability of cell membranes, which plays an essential role in the biosynthesis and metabolism of bile acid, cellular signaling, cellular integrity during stress,<sup>[7]</sup> and mass transfer.<sup>[8]</sup> Tumor cells accumulate high levels of cholesterol via both enhanced receptor-mediated endocytosis of cholesterol-binding low-density lipoproteins and upregulated cholesterol synthesis by acetyl coenzyme A (AcCoA) through a “mevalonate metabolism” in the endoplasmic reticulum (ER).<sup>[9]</sup> The abnormally high cholesterol level in cancerous tissues is pro-tumorigenic.<sup>[10]</sup> Recent studies have further shown that intratumorally enriched cholesterol increases ER stress of tumor-infiltrating T cells and induces exhaustion of effector functions with upregulated immune checkpoints; thus, creating an immunosuppressive tumor microenvironment (TME).<sup>[11]</sup> Although immune checkpoint blockade (ICB) with anti-PD-(L)1 and anti-CTLA4 antibodies have revolutionized the treatment of a small subset of cancer patients, ICB does not benefit patients with immunologically “cold” tumors due to insufficient antigen presentation and sparse immune infiltration.<sup>[11]</sup> As a result, depletion of cholesterol can potentially influence the cell membrane stability, reinvigorate T cells, and induce immunogenic TME for

## 1. Introduction

The mechanical tension of cell membranes,<sup>[1]</sup> defined as the force per unit length acting on a cross-section of phospholipid

W. Zhen, T. Luo, Z. Wang, X. Jiang, E. Yuan, W. Lin  
Department of Chemistry  
The University of Chicago  
Chicago, IL 60637, USA  
E-mail: wenbinlin@uchicago.edu

W. Zhen, X. Jiang, R. R. Weichselbaum, W. Lin  
Department of Radiation and Cellular Oncology  
The Ludwig Center for Metastasis Research  
The University of Chicago  
Chicago, IL 60637, USA

 The ORCID identification number(s) for the author(s) of this article can be found under <https://doi.org/10.1002/smll.202305440>

© 2023 The Authors. Small published by Wiley-VCH GmbH. This is an open access article under the terms of the Creative Commons Attribution License, which permits use, distribution and reproduction in any medium, provided the original work is properly cited.

DOI: 10.1002/smll.202305440

synergistic antitumor effects when combined with other therapeutic modalities. However, it remains unclear how the altered cholesterol content regulates the membrane mechanical properties and physiological activities of cancer cells.

Herein, we report our findings that cholesterol depletion by cholesterol oxidase (COD) increases the membrane tension of cancer cells, re-assembles the cytoskeleton, raises the osmotic pressure inside the cell, and increases rupture susceptibility from external stimuli, including hypotonic shock and oxidative stress. Based on these findings, we designed a COD-functionalized nanoscale metal–organic framework (MOF), Hf-TBP/COD, to achieve synergistic anticancer effects via COD-induced cholesterol depletion and Hf-TBP-mediated reactive oxygen species (ROS) generation. Hf-TBP is comprised of Hf<sub>6</sub> secondary building units (SBUs) and photosensitizing 5,10,15,20-tetra(p-benzoato)porphyrin (TBP) ligands. COD is adsorbed onto Hf-TBP to afford Hf-TBP/COD, which depletes cholesterol and produces H<sub>2</sub>O<sub>2</sub>, thereby enhancing antitumor effects of Hf-TBP-mediated photodynamic therapy (PDT). Depletion of cholesterol in the TME also downregulates immunosuppressive checkpoints to reinvigorate T cells. Hf-TBP/COD plus light irradiation demonstrates strong antitumor effects in murine triple-negative breast cancer 4T1 and murine colon adenocarcinoma MC38 models. Hf-TBP/COD plus light irradiation also significantly enhances antitumor immune responses via simultaneous reinvigoration of T-cells and enhancement of cancer cell pyroptosis.

## 2. Results and Discussion

### 2.1. Cholesterol Depletion Regulates the Mechanical Tension of Cancer Cell Membranes

We first investigated how cholesterol regulation affected the activities of cancer cells with the goal of finding novel strategies for cancer treatment. We chose the enzyme COD to regulate cholesterol content because it could catalytically convert cholesterol and oxygen to cholest-5-en-3-one and hydrogen peroxide (Figure S1, Supporting Information). The murine mammary carcinoma cell line (4T1) with a fusiform-like shape was used in the initial studies to infer the impact of cholesterol regulation based on cell morphology changes.<sup>[12]</sup> The cholesterol level in 4T1 cells was analyzed with Filipin III by flow cytometry,<sup>[11b]</sup> which decreased steadily with an increasing concentration of COD. Quantification of mean Filipin III fluorescence revealed a 77.3% decrease of cholesterol after incubation of 4T1 cells with 0.125 unit mL<sup>-1</sup> COD for 24 h (Figure 1a; Figure S2, Supporting Information). We also detected the byproduct of COD-catalyzed cholesterol oxidation, H<sub>2</sub>O<sub>2</sub> (Figure 1b; Figure S3, Supporting Information). At a COD concentration of 0.125 unit mL<sup>-1</sup>, the mean intracellular 2',7'-dichlorodihydrofluorescein (DCFH) signal increased by 42.7% over PBS control.

Cholesterol is maintained above a critical level to physiologically stabilize cell membranes. We studied how COD treatment affected 4T1 cell membrane tension. Hypo-osmotic shock is commonly used to induce mechanical stress on cell membranes. We assessed the rupture of cholesterol-depleted 4T1 cells by measuring the percentages of lactate dehydrogenase (LDH) release.<sup>[13]</sup> In the structurally stable cancer cells, hypo-osmotic shock of culturing in 0.125× PBS for 30 min slightly increased the rupture

ratio to 18% from 9.8% for PBS control. In contrast, cholesterol depletion by 0.125 unit mL<sup>-1</sup> COD drastically increased the rupture ratio to 90%, suggesting COD increased the osmotic fragility of cancer cell membranes (Figure 1c).

We used confocal laser scanning microscopy (CLSM) to observe 4T1 cell morphology changes during this process. Upon a short-term hypo-osmotic shock or stimulation with a lysis solution, PBS treatment showed no obvious impact on cell morphology, but COD treatment reduced the bright field contrast (Figure 1d; Figure S4, Supporting Information), which suggests a diminished refractive index difference between the interiors and exteriors of 4T1 cells due to rapid solute equilibration. We next explored if COD treatment impacted the cytoskeleton by observing the changes in F-actin expression (Figure 1e; Figure S5, Supporting Information). Co-culturing with hypotonic solutions (0.5 and 0.25 × PBS, 30 min) or a lysis solution for 1 min did not cause apparent alteration of F-actin assembly in PBS-treated 4T1 cells but significantly decreased the F-actin assembly in the centers and increased the F-actin signals at the peripheries of COD-treated cells.<sup>[2]</sup> In addition, typical uniform F-actin distribution changed to clusters and spots in COD-treated 4T1 cells. Stimulation with hypotonic solutions for 30 min further reduced cytoplasmic fluorescence, suggesting that cholesterol depletion compromised cancer cell membranes and redistributed F-actin in the cells.

We next used fluorescence-lifetime imaging microscopy (FLIM) to probe the impact of cholesterol depletion on mechanical tension of cell membranes. Flipper-TR has been shown to be an excellent fluorescence probe to sense the tension between lipid layers through a change of the twist angle between two dithienothiophenes; and hence, the fluorescence signal of Flipper-TR.<sup>[14]</sup> Hypotonic conditions slightly increased membrane tension<sup>[15]</sup> of 4T1 cells as demonstrated by color-coded average lifetime maps (Figure 1f) and increased average fluorescence lifetimes of Flipper-TR from 0.36 ± 0.03 ns to 0.46 ± 0.04 ns for  $\tau_1$  and 4.22 ± 0.12 ns to 4.43 ± 0.10 ns for  $\tau_2$ . In comparison, a significant increase of cell membrane tension was observed in COD-treated cells with a  $\tau_1$  of 0.57 ± 0.08 ns and a  $\tau_2$  of 4.63 ± 0.07 ns. The increased fluorescence lifetimes of Flipper-TR in COD-treated cells were confirmed by time-dependent fluorescence decay curves (Figure 1h,i; Figures S6–S8, Supporting Information). The increased membrane tension suggested that the repolymerized F-actin around the membrane might be caused by the increased cell permeability and rapid solute diffusion through the membranes. The mechanical tension of cell membranes was also related to mechano-sensitive ion channels (MSCs) and cell mechano-transduction, which could lead to depolarization of cell membrane potential and eventual cell lysis through osmotic imbalance. CLSM imaging by Fluo 3-AM staining revealed that more calcium ions entered cholesterol-depleted 4T1 cells (Figure 1g).

As the structural stability and mechanical tension of cell membranes affect cancer cell invasion and metastasis, scratch wound analysis was conducted to evaluate the invasion of 4T1 cells using an InCuCyte S3 live imaging system.<sup>[16]</sup> Compared with the initial wound areas, COD treatment reduced the percentage of wound closures (Figure 1j; Figure S9, Supporting Information), indicating the increased cell membrane mechanical tension reduced the invasiveness of 4T1 cells. Interestingly, cholesterol-depleted 4T1 cells were more vulnerable to cytotoxicity caused

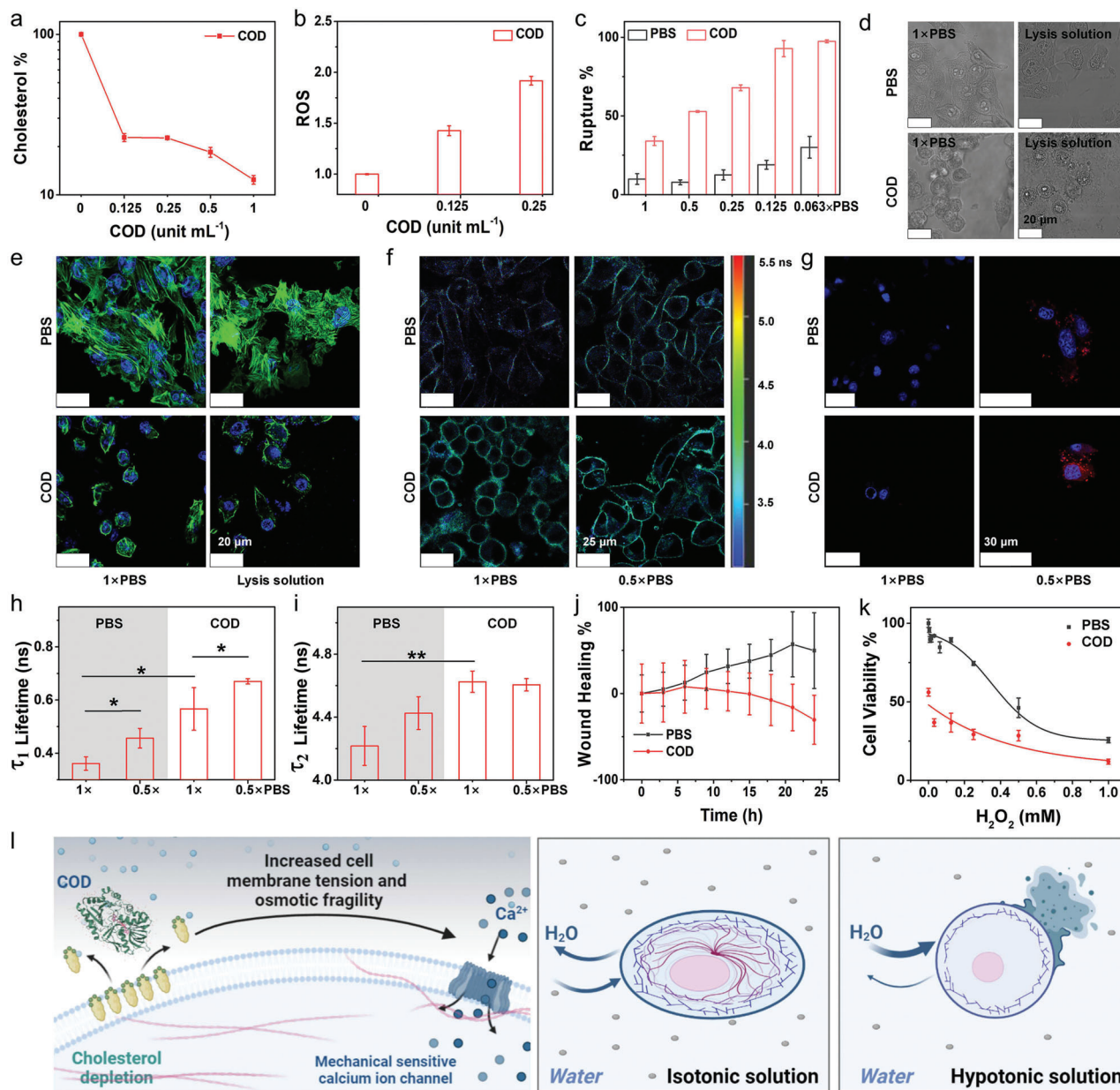


**Figure 1.** a) Depletion of cholesterol in 4T1 cells by COD probed by Filipin III ( $n = 3$ ). b) COD-induced ROS generation in 4T1 cells ( $n = 3$ ). c) Rupture ratios of PBS- and COD-treated 4T1 cells (0.06 unit  $\text{mL}^{-1}$  for 12 h) after incubation with hypotonic solutions (0.5 $\times$ , 0.25 $\times$ , 0.125 $\times$ , and 0.063 $\times$  PBS) for 30 min ( $n = 3$ ). d) Morphology changes of PBS- and COD-treated 4T1 cells (0.06 unit  $\text{mL}^{-1}$  for 12 h) after incubation with hypotonic solutions (0.5 $\times$ , 0.25 $\times$  PBS) for 30 min or lysis solution for 1 min. e) F-actin cytoskeleton assemblies of 4T1 cells pre-incubated with PBS or COD (COD: 0.06 unit  $\text{mL}^{-1}$ ) for 12 h followed by incubation with PBS solutions (1 $\times$  PBS) for 30 min or lysis solution for 1 min. f) Color-coded average lifetime maps for evaluating the plasma membrane mechanical tension of PBS- and COD-treated 4T1 cells after incubation with 1 $\times$  PBS or hypotonic solution (0.5 $\times$  PBS) as probed by Flipper-TR lifetimes. g) Influx of calcium ions in 4T1 cancer cells after different treatments. h)  $\tau_1$  lifetime and i)  $\tau_2$  lifetime of Flipper-TR in 4T1 cells after PBS, 0.5 $\times$  PBS, COD, and COD + 0.5 $\times$  PBS treatments ( $n = 3$ , \*,  $p < 0.05$ ; \*\*,  $p < 0.01$ ). j) Time-dependent wound healing of 4T1 cells post PBS or COD treatment ( $n = 3$ ). k) Cell viability of PBS- and COD-treated 4T1 cells (0.06 unit  $\text{mL}^{-1}$  for 12 h) after incubation with different concentrations of  $\text{H}_2\text{O}_2$  for 30 min ( $n = 3$ ). l) Schematic depicting how cholesterol depletion increases cell membrane mechanical tension and osmotic fragility to stimulate influx of calcium ions and increase rupture of cancer cells after incubation with hypotonic solutions.

by hydrogen peroxide ( $\text{H}_2\text{O}_2$ , Figure 1k). Taken together, COD effectively depletes cholesterol on cancer cell membranes, increases the mechanical tension and osmotic fragility of plasma membranes, raises intracellular osmotic pressure due to opening of mechanically sensitive ion channels, and inhibits 4T1 cell

migration. As a result, 4T1 cells are more likely to be lysed by external mechanical pressures and killed by ROS (Figure 1l). Based on these findings, we hypothesized that cell membrane tension regulation by COD could be combined with ROS-generating therapies to achieve synergistic anticancer effects.

## 2.2. Preparation and Characterization of Hf-TBP/COD

Based on our observations that COD-mediated cholesterol depletion increases the mechanical tension of cell membranes and 4T1 cell susceptibility to ROS-induced cytotoxicity, we hypothesized that cholesterol depletion could be combined with PDT to synergistically enhance their anticancer effects. We further surmised that Hf-TBP could not only act as a biocompatible carrier for COD delivery but also provide an excellent nanophotosensitizer for effective PDT. As a non-invasive and localized treatment, PDT uses light, photosensitizers (PSs), and molecular oxygen to generate ROS to kill cancer cells.<sup>[17]</sup> Many reports suggest that PDT can trigger pyroptosis rather than apoptosis for TME activation.<sup>[18]</sup> As most molecular PSs are highly conjugated with low solubility and a tendency for aggregation-induced quenching of photoexcited states, nanotechnology has provided a potential solution to overcome these limitations. In particular, nanoscale MOFs have emerged as a novel class of nanophotosensitizers with excellent PDT efficacy.<sup>[19]</sup> MOF-based nanophotosensitizers exhibit tunable compositions to accommodate different molecular PSs, crystalline frameworks to minimize excited-state quenching, and high payloads of PSs for efficient delivery to tumors.<sup>[20]</sup> In addition to improved PDT efficacy over conventional PSs, MOFs also have porous structures and dynamic surfaces for loading therapeutic agents or molecules with different physicochemical properties and to facilitate their retention in tumor tissues and uptake by cancer cells.<sup>[20]</sup>

Hf-TBP MOF based on Hf<sub>6</sub>-SBUs and TBP ligands was chosen for this study owing to its good biocompatibility and moderate PDT efficacy.<sup>[21]</sup> Hf-TBP was synthesized via a solvothermal reaction between HfCl<sub>4</sub> and 5,10,15,20-tetra(p-benzoato)porphyrin (H<sub>4</sub>TBP) in *N,N*-dimethylformamide with formic acid as the modulator at 125 °C for 2 days (Figure 2a).<sup>[21]</sup> Hf-TBP adopted the reported MOF-545 structure with Hf<sub>6</sub>(μ<sub>3</sub>-O)<sub>4</sub>(μ<sub>3</sub>-OH)<sub>4</sub> SBUs based on their powder X-ray diffraction (PXRD) patterns (Figure 2b).<sup>[22]</sup> The ratio of Hf to TBP was determined to be 3.3 in Hf-TBP by inductively coupled plasma-mass spectrometry (ICP-MS) and ultraviolet–visible (UV–vis) spectroscopy (Figure S10, Supporting Information), affording an empirical formula of (μ<sub>3</sub>-O)<sub>4</sub>(μ<sub>3</sub>-OH)<sub>4</sub>(OH)<sub>4</sub>(HCO<sub>2</sub>)<sub>0.6</sub>(TBP)<sub>1.85</sub>. Hf-TBP had large 1D channels with a size of 3.6 nm (Figure S11, Supporting Information). Bicinchoninic acid assay showed that COD could be loaded in Hf-TBP via physical adsorption at room temperature for 6 h (Figure 2a; Figure S12, Supporting Information),<sup>[23]</sup> and the loading efficiency could reach as high as 56.1%.

Transmission electron microscopy (TEM) images revealed the nano-rice morphology of Hf-TBP and Hf-TBP/COD with lengths of 70–200 nm and widths of 30–0 nm (Figure 2c; Figure S13, Supporting Information). In addition, Hf-TBP/COD exhibited unchanged PXRD patterns from Hf-TBP, indicating the stability of Hf-TBP during the COD loading process (Figure 2b).<sup>[23]</sup> As the isoelectric points of arginine (Arg, R), histidine (His, H), and lysine (Lys, K) of COD are 10.76, 7.59, and 9.74 (Figure S14 and Table S1, Supporting Information), respectively, these amino acids residues bear positive charge during loading process in Hf-TBP aqueous solution, and there will be attractive electrostatic interactions between these positive amino acid residues and negative charged Hf-TBP. In addition, the amino and carboxylate groups in COD can bind to the surface of Hf-TBP via hydro-

gen bonds (Figure S14, Supporting Information). The loading of COD in Hf-TBP was supported by the appearance of the characteristic C–H stretching peak at ≈2908 cm<sup>-1</sup> of COD in the Fourier-transform infrared spectroscopy (FT-IR) spectra of Hf-TBP/COD (Figure 2d). Both Hf-TBP and Hf-TBP/COD showed good dispersibility in water with average hydrodynamic diameters of 91.28 and 105.7 nm (Figure 2e) and ζ-potentials of -24.9 and -10.19 mV, respectively (Figure 2f); the increased hydrodynamic diameter and zeta potential of Hf-TBP/COD suggested the COD could be adsorbed onto the surface of Hf-TBP.<sup>[24]</sup> The release of COD from Hf-TBP/COD was evaluated in physiologically relevant environments. Approximately 10.3% and 7.0% of COD were released in PBS at pH 5.0 and pH 7.4, respectively, over 48 h (Figure 2g; Figure S15, Supporting Information). Light irradiation (100 mW cm<sup>-2</sup>, 15 min) did not increase COD release (6.6%). The DCFH assay showed significantly higher ROS signals from Hf-TBP/COD under light irradiation (660 nm, 100 mW cm<sup>-2</sup>), suggesting the PDT capability of TBP in Hf-TBP/COD (Figure 2h).<sup>[25]</sup>

## 2.3. Hf-TBP/COD Changes the Mechanical Tension of Cancer Cell Membranes

We then determined how Hf-TBP/COD interacted with cancer cells and exerted their therapeutic effects. Flow cytometric analysis of TBP showed that Hf-TBP/COD exhibited a slightly lower cellular uptake than Hf-TBP (Figure S16 and Table S2, Supporting Information), which could be mediated by COD-induced membrane tension which inhibited endocytosis by counteracting clathrin polymerization and activating membrane fission.<sup>[26]</sup> The cholesterol level also decreased steadily with an increasing concentration of Hf-TBP/COD (Figure 2i), while the cholesterol level in Hf-TBP treated cells did not show significant change (Figure S17, Supporting Information). We also detected the byproduct of COD-catalyzed cholesterol oxidation, H<sub>2</sub>O<sub>2</sub>, by DCFH-DA. Without light illumination, Hf-TBP/COD elevated ROS levels in 4T1 cells (Figure 2j; Figure S18, Supporting Information), while Hf-TBP had a slight effect on ROS generation. These results indicate that the biocatalytic activity of COD was maintained after loading onto Hf-TBP due to the mild condition in the aqueous media.<sup>[27]</sup> Upon binding to the surface of cells, loaded COD could deplete cholesterol from phospholipid bilayers and compromise the integrity of the cancer cell membrane, which was supported by the increased LDH release from Hf-TBP/COD treatment (Figure 2k). We next studied the stability of cell membranes and the susceptibility of 4T1 cells to lysis. 4T1 cells pre-incubated with Hf-TBP/COD showed a higher rupture ratio when treated with an ammonium-chloride-potassium (ACK) buffer (Figure 2l) or hypotonic solutions (Figure 2m), suggesting the Hf-TBP/COD delivered COD to decrease the membrane stability with increased osmotic fragility.

We next studied cell membrane mechanical tension and ROS resistance of Hf-TBP/COD-treated 4T1 cells. Hf-TBP/COD-treated cells showed an obvious loss of bright field contrast (Figure 3a; Figure S19, Supporting Information), an apparent decrease of the F-actin assembly in the center of the cell and an increase of the F-actin signal at the periphery (Figure 3b; Figure S20, Supporting Information), and an influx of calcium

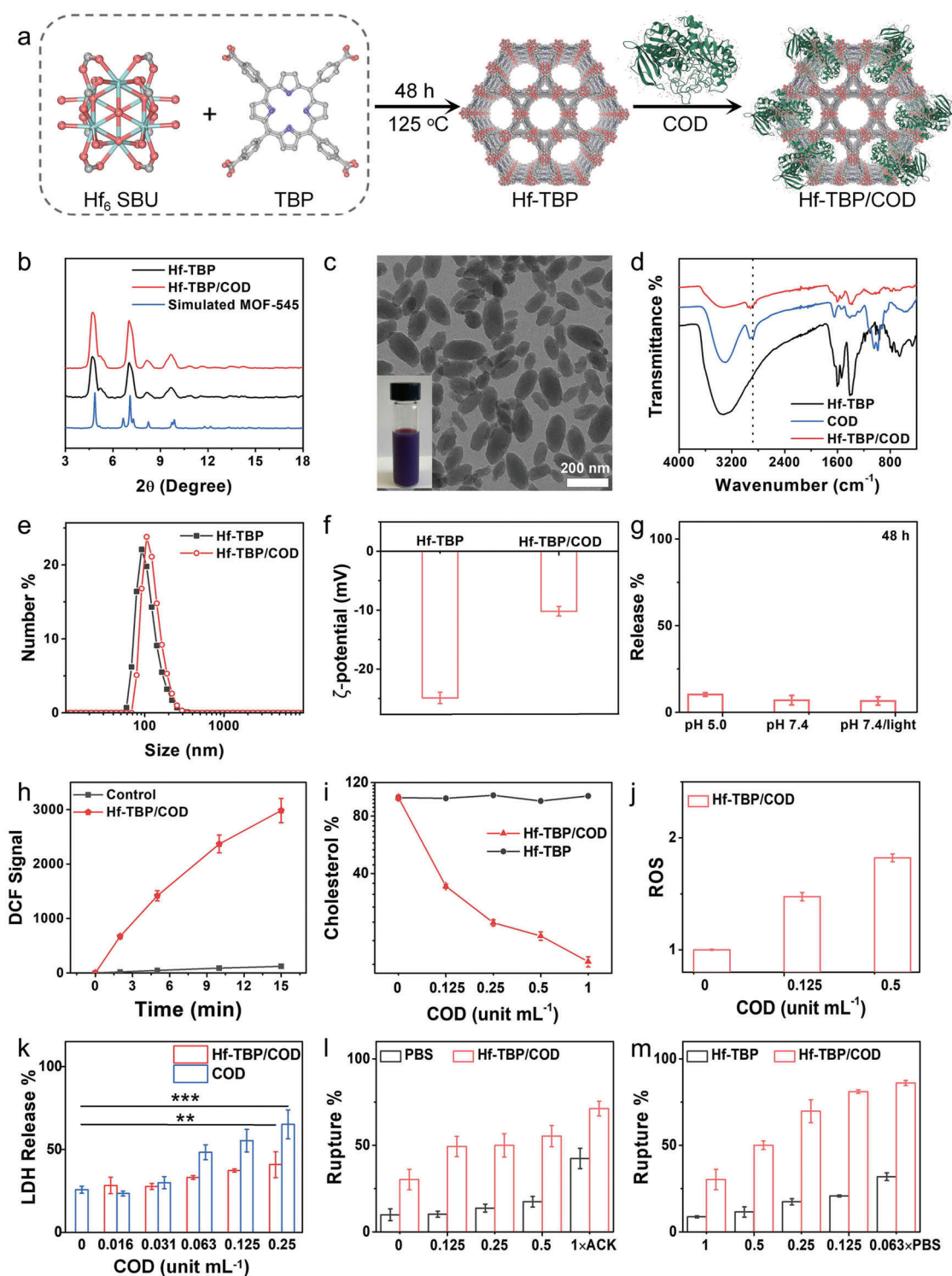


**Figure 2.** a) Synthetic scheme of Hf-TBP and Hf-TBP/COD. b) PXRD patterns of Hf-TBP, Hf-TBP/COD, and the simulated pattern of MOF-545. c) TEM image of Hf-TBP/COD (inset: photograph of a Hf-TBP/COD dispersion in water). d) FT-IR spectra of Hf-TBP, COD, and Hf-TBP/COD. e) Hydrodynamic sizes and f)  $\zeta$ -potentials of Hf-TBP and Hf-TBP/COD in water. g) Release of COD from Hf-TBP/COD. h) ROS generation under 660 nm light irradiation by DCFH assay ( $100 \text{ mW cm}^{-2}$ ). i) Depletion of cholesterol in 4T1 cells by different concentrations of Hf-TBP/COD. j)  $\text{H}_2\text{O}_2$  generation with the catalysis of COD in Hf-TBP/COD. k) Percentages of LDH release from 4T1 cells after incubation with COD or Hf-TBP/COD at different concentrations. l) Rupture ratios of 4T1 cancer cells pre-incubated with Hf-TBP/COD for 12 h followed by incubation with 0.125 $\times$ , 0.25 $\times$ , 0.5 $\times$ , or 1 $\times$  ACK solution for 30 min. m) Rupture ratios of 4T1 cancer cells pre-incubated with Hf-TBP/COD for 12 h followed by incubation with 0.063 $\times$ , 0.125 $\times$ , 0.25 $\times$ , 0.5 $\times$ , or 1 $\times$  PBS solution for 30 min.  $n = 3$  for (e–m). \*,  $p < 0.05$ ; \*\*,  $p < 0.01$ ; and \*\*\*,  $p < 0.001$ .

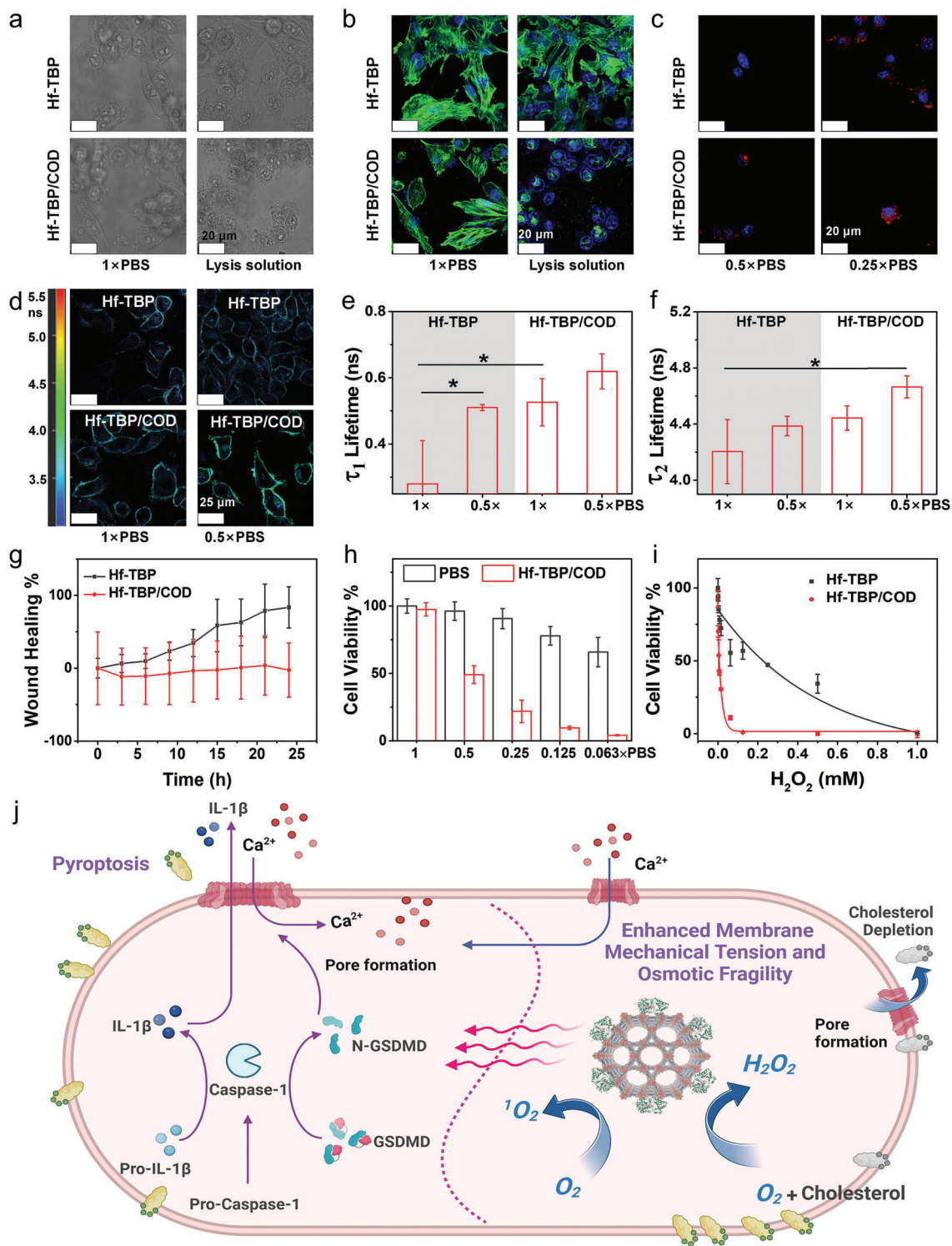


**Figure 3.** a) Morphology changes and b) F-actin cytoskeleton assemblies of 4T1 cells pre-incubated with Hf-TBP or Hf-TBP/COD (COD: 0.06 unit mL<sup>-1</sup>) for 12 h followed by incubation with lysis solution for 1 min. c) Influx of calcium ions in 4T1 cancer cells after different treatments. d) Plasma membrane mechanical tension of 4T1 cells after different treatments, as probed by Flipper-TR lifetimes. e)  $\tau_1$  and f)  $\tau_2$  lifetime of Flipper-TR in 4T1 cells after different treatments. g) Time-dependent wound healing of 4T1 cells post Hf-TBP or Hf-TBP/COD. h) Cell viability of 4T1 cancer cells pre-incubated with Hf-TBP/COD for 12 h followed by incubation with hypotonic solutions. i) Cell viability of 4T1 cancer cells pre-incubated with Hf-TBP/COD for 12 h followed by incubation with different concentrations of  $H_2O_2$ . j) Proposed therapeutic mechanisms of Hf-TBP/COD. Cholesterol depletion and  $H_2O_2$  production during COD-catalyzed cholesterol oxidation reduces the tolerance of cancer cells to ROS and lysis and enhances caspase-1-mediated pyroptosis.  $n = 3$  for (e–i), \*,  $p < 0.05$ ; \*\*,  $p < 0.01$ ; \*\*\*,  $p < 0.001$ ; and \*\*\*\*,  $p < 0.0001$ .

ions (Figure 3c) in response when treated with hypotonic solutions. In contrast, Hf-TBP-treated cells did not show any difference from PBS control. In addition, hypotonic conditions slightly increased membrane tension of Hf-TBP-treated cells,<sup>[28]</sup> while Hf-TBP/COD-treated cells increased  $\tau_1$  and  $\tau_2$  values to  $0.53 \pm 0.12$  ns and  $4.44 \pm 0.09$  ns, respectively, from  $0.36 \pm 0.03$  ns and  $4.22 \pm 0.12$  ns, respectively for PBS control (Figure 3d–f; Figures S21 and S22, Supporting Information). Scratch wound healing experiments also suggested that Hf-TBP/COD could successfully reduce the percentage of wound closures (Figure 3g; Figure S23, Supporting Information), suggesting the potential of inhibiting tumor metastasis. We also found 4T1 cells pre-incubated with Hf-TBP/COD were more vulnerable to hypotonic solutions (Figure 3h) and externally added  $H_2O_2$  (Figure 3i).

We hypothesized that Hf-TBP/COD-induced cholesterol depletion and increased cell membrane tension might enhance the PDT effect and pyroptosis of cancer cells (Figure 3j). Pyroptosis is a newly defined type of programmed cell death<sup>[10]</sup> characterized by rapid membrane rupture accompanied by cell swelling with large bubbles and release of damage-associated molecular patterns (DAMPs) and is usually triggered by inflammatory caspase-1-mediated gasdermin D (GSDMD) cleavage.<sup>[18a,29–31]</sup>

#### 2.4. Stimulation of Pyroptosis and Induction of Immunogenic Cell Death

The intracellular PDT effects of Hf-TBP and Hf-TBP/COD were evaluated under 660 nm light irradiation (denoted Hf-TBP(+) and Hf-TBP/COD(+)); Hf-TBP/COD(+) showed a much higher intracellular ROS level than Hf-TBP(+) alone due to the produced  $H_2O_2$  catalyzed by COD (Figure 4). We next detected the activation of caspase-1 by various treatments. Hf-TBP/COD(+) showed enhanced activation of pyroptosis associated with higher caspase-1 expression to trigger potent inflammatory responses over Hf-TBP(+) (Figure 4b; Figure S24, Supporting Information), likely due to synergistic actions of the enhanced PDT effect and COD-mediated cell membrane rupture via cholesterol depletion. Active caspase-1 cleaves GSDMD (Figure 4d; Figure S25, Supporting Information) at a link between its N-terminal and C-terminal domains. Hf-TBP/COD(+)-treated cells showed a higher cleavage ratio of GSDMD than Hf-TBP(+) group, suggesting that cholesterol depletion provides a novel avenue to enhance pyroptosis of cancer cells. (Figure 3j). By forming membrane pores, GSDMD-N elicits cell death and activates the release of cytosolic IL-1 $\beta$  (Figure 4c).<sup>[30,31]</sup> The enhanced pyroptosis by Hf-TBP/COD(+) was supported by its higher percentage of LDH release from 4T1 cells than that of Hf-TBP(+) treatment (Figure 4g).

To further probe if Hf-TBP/COD(+) could stimulate pyroptosis, we determined the morphology change of cancer cells by CLSM. Different from the cells treated with Hf-TBP/COD, COD(+), or Hf-TBP(+), 4T1 cells treated with Hf-TBP/COD(+) displayed a distinctive morphology with a swollen cell shape and large bubbles blowing from plasma membranes, suggesting efficient stimulation of pyroptosis (Figure 4e; Figure S26, Supporting Information).<sup>[30d,31]</sup> Time-lapse videos were also generated using bright-field images to show the morphology changes. Under laser irradiation, the membranes of cancer cells pre-incubated with Hf-TBP/COD exhibited a more pronounced

pyroptotic morphology and a faster bubbling rate than cells pre-incubated with Hf-TBP (Videos S1 and S2, Supporting Information), which supported cholesterol depletion from the phospholipid bilayers. The time-lapse videos also showed the disappearance of green fluorescence from the cytoplasm and the staining of cell nuclei with propidium iodide (PI, red color), indicating the synergistic actions of Hf-TBP-mediated PDT and COD-mediated cholesterol depletion in enhancing cell membrane disruption and pyroptosis of cancer cells. Similar to the effect of hypotonic shock, PDT-initiated pyroptosis caused cell membrane damage to stimulate the influx of calcium ions (Figure 4f). Further, Hf-TBP/COD(+)-treated cells showed a lower wound healing effect than Hf-TBP(+)-treated cells, likely a result of reduced cell adhesion and migration as result of increased mechanical tension of cell membranes (Figure 4h,i; Figure S27, Supporting Information). It also had higher cytotoxicity than Hf-TBP(+), with half-maximal inhibitory concentrations ( $IC_{50}$ ) decreasing from 35.0 to 10.8  $\mu$ M and from 12.8 to 1.2  $\mu$ M in 4T1 and MC38 cells (Figure 4j,k), respectively. No toxicity was observed for cells treated with up to 25  $\mu$ M Hf-TBP without light irradiation (Figure S28, Supporting Information), and slight toxicity in the Hf-TBP/COD group (Figure S29, Supporting Information) could be attributed to cholesterol depletion by the loaded COD in Hf-TBP/COD (Figures S17 and S30, Supporting Information).

Compared to apoptosis, pyroptosis is more immunogenic and can release tumor antigens and DAMPs more efficiently to elicit robust innate immune activation and turn immunologically “cold” TME “hot.”<sup>[30]</sup> Next, we examined immunogenic cell death (ICD) of 4T1 cells by flow cytometry. The synergy between cholesterol depletion and PDT successfully induced surface translocation of calreticulin (CRT, Figure 4l; Figure S31, Supporting Information), which serves as an “eat-me” signal and stimulates phagocytosis by macrophages and dendritic cells (DCs).<sup>[31]</sup> Hf-TBP/COD(+) upregulated phosphatidylserine on cell membranes by Annexin-V staining and impaired cell membrane function with influx of cell-impermeable PI via pyroptosis (Figure 4m; Figure S32, Supporting Information). DCs represent the sentinels of the immune system and play an important role in linking innate and adaptive immune responses.<sup>[32]</sup> We quantified the maturation of bone marrow-derived dendritic cells (BMDCs) with activation markers CD80/CD86 by flow cytometry (Figure 4n; Figure S33, Supporting Information).<sup>[33]</sup> Hf-TBP/COD and COD(+) slightly stimulated DC maturation from 6.03% for PBS to 7.17% and 12.5%, respectively, which suggested the cholesterol depletion alone could trigger the immunogenicity of the TME to a certain extent. Compared to the percentage of mature DCs (8.35%) in the Hf-TBP(+) group, significantly more DCs (28.75%) were activated after incubation with Hf-TBP/COD(+)-treated 4T1 cells (Figure 4n). Thus, Hf-TBP/COD(+) realized effective killing of cancer cells and induced robust ICD for antigen presenting cell activation.<sup>[34]</sup>

#### 2.5. Cholesterol Depletion Downregulates Immune Checkpoints and Stimulates Adaptive Immune Responses

Recent studies suggest that high levels of cholesterol exhaust T cells via upregulating immunosuppressive checkpoints such as PD-1, 2B4, TIM-3, and LAG-3 (Figure 5a).<sup>[11b]</sup> We first tested the

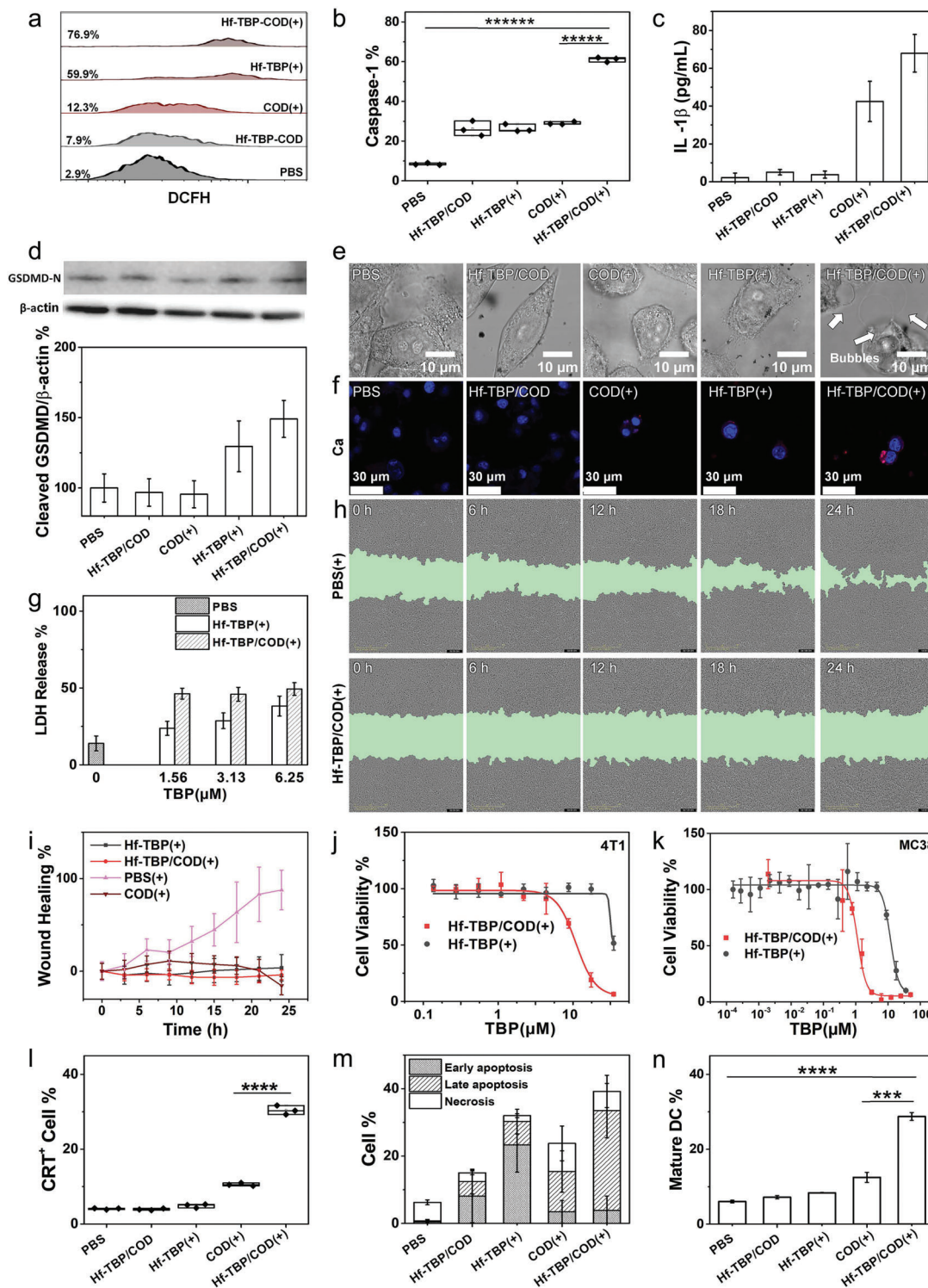


**Figure 4.** a) In vitro ROS generation after 660 nm light irradiation ( $90 \text{ J cm}^{-2}$ ) detected by DCFH-DA. b) Expression levels of caspase-1 in 4T1 cells after 660 nm light irradiation ( $90 \text{ J cm}^{-2}$ ,  $n = 3$ ). c) Secretion of IL-1 $\beta$  from 4T1 cells after different treatments ( $90 \text{ J cm}^{-2}$ ) ( $n = 3$ ). d) Cleavage of GSDMD in 4T1 cells after 660 nm light irradiation ( $90 \text{ J cm}^{-2}$ ) ( $n = 3$ ). e) Morphology changes of 4T1 cells induced by pyroptosis after PDT treatment ( $90 \text{ J cm}^{-2}$ ). f) Calcium ions influx after different treatments. g) Percentages of LDH release from 4T1 cells after different treatments ( $90 \text{ J cm}^{-2}$ ) ( $n = 3$ ). h, i) Time-dependent wound healing percentages after different treatments ( $n = 3$ ). Viabilities of j) 4T1 and k) MC38 cells after Hf-TBP(+) or Hf-TBP/COD(+) treatment ( $n = 3$ ). l) Percentages of CRT-positive 4T1 cells after different treatments ( $n = 3$ ). m) Percentages of 4T1 cells in the early apoptosis, late apoptosis, and necrosis states detected by flow cytometry ( $n = 3$ ). n) Percentages of mature DCs (CD80<sup>+</sup> CD86<sup>+</sup>) detected by flow cytometry ( $n = 3$ ). \*,  $p < 0.05$ ; \*\*,  $p < 0.01$ ; \*\*\*,  $p < 0.001$ ; and \*\*\*\* and  $p < 0.0001$ .



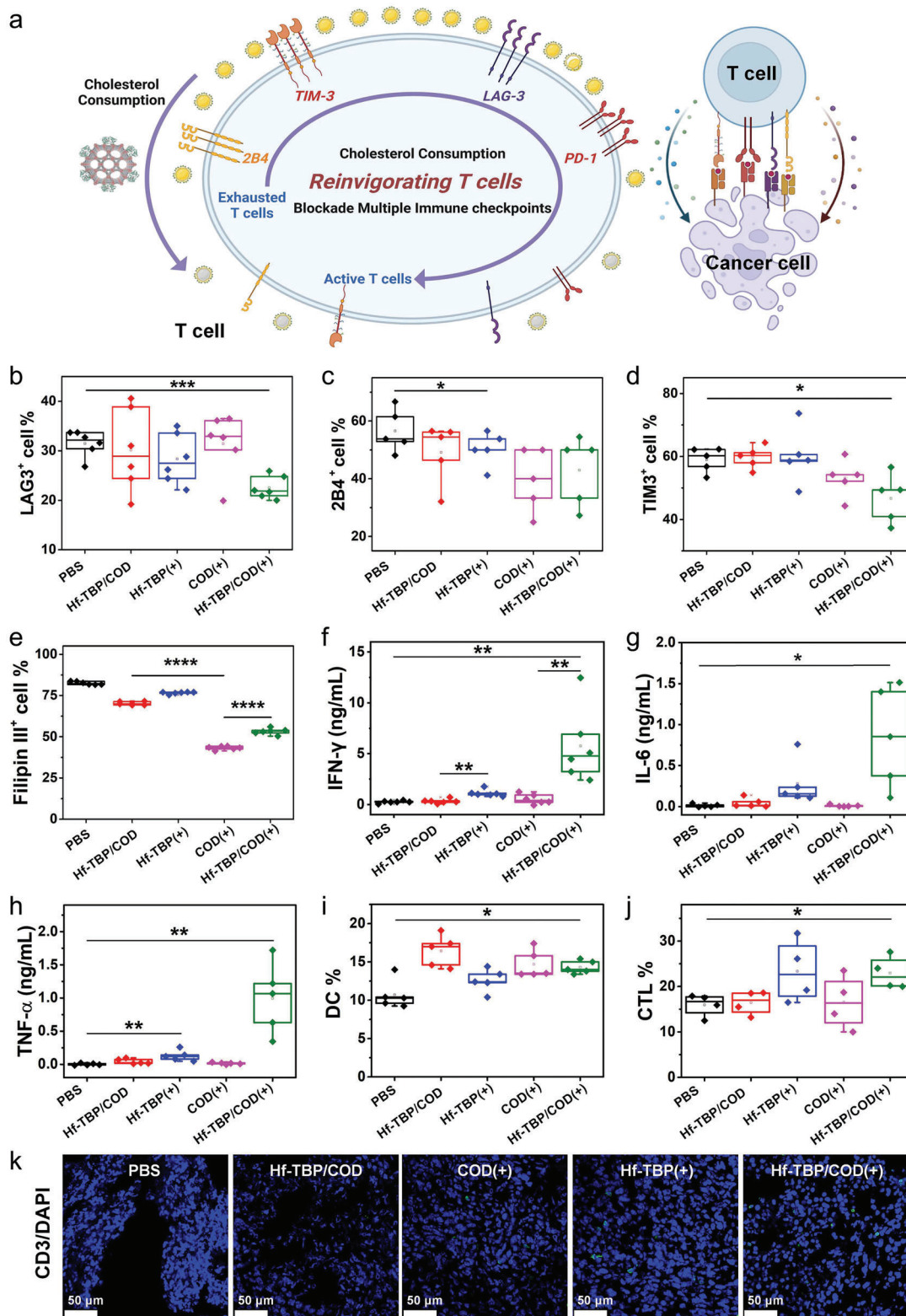


**Figure 5.** a) Schematic showing proposed mechanisms of immune checkpoint downregulation by Hf-TBP/COD. Loaded COD could consume the cholesterol in TME and downregulate the expression of immunosuppressive checkpoints such as PD-1, 2B4, TIM-3, and LAG-3 in T cells. Upon light irradiation, tumor cells underwent caspase-1-mediated pyroptosis and released DAMPs and tumor-associated antigens, which turned the TME "hot." Through this process, DC maturation and antigen presentation were enhanced, and activated T cells infiltrated into tumors and functioned within a cholesterol-depleted TME, avoiding T-cell exhaustion and tumor resistance. Expression levels of immune checkpoints including b) LAG3, c) 2B4, and

biocompatibility of Hf-TBP/COD with immune cells by examining the toxicity of Hf-TBP/COD on splenocytes. MTS assays showed no obvious changes in cell viabilities when incubated with Hf-TBP/COD at an equivalent COD concentration of 1 unit mL<sup>-1</sup>, suggesting that Hf-TBP/COD is non-toxic to splenocytes, including T cells (Figures S34 and S35, Supporting Information). We next measured the hemolytic effect of Hf-TBP/COD through a hemolysis assay. Hf-TBP/COD caused 1.57% hemolysis of red blood cells (extracted from BALB/c mice) at an equivalent TBP concentration of 100 μM (Figure S36, Supporting Information). This result supported the biocompatibility of Hf-TBP/COD with normal cells.<sup>[35]</sup> To probe if Hf-TBP/COD could inhibit T-cell exhaustion, we detected expression levels of immune checkpoints in the TME after treatment of MC38 tumor-bearing C57BL/6 mice with Hf-TBP/COD(+). COD treatment showed obvious downregulation of 2B4, TIM-3, and PD-1, suggesting effective downregulation of these immunosuppressive checkpoints via depleting cholesterol in the TME (Figure 5b–d; Figures S37–S40, Supporting Information). Interestingly, Hf-TBP/COD(+) treatment further downregulated 2B4, TIM-3, and LAG3 expressions (Figure 5b–d), likely due to the additional impact of PDT on tumor metabolism.<sup>[35b,36]</sup> Unlike immune checkpoint inhibitors currently employed in the clinic, which generally inhibit one checkpoint with one antibody, cholesterol depletion in the TME (Figure 5e; Figure S41, Supporting Information) downregulates multiple immune checkpoints simultaneously, which may amplify immune responses and enhance the therapeutic effects of PDT (Figure 5a).

We next examined the effects of Hf-TBP/COD(+)-mediated PDT, cholesterol depletion, and immunosuppressive checkpoint downregulation on the stimulation of immune responses by evaluating the release of inflammatory cytokines and activation of immune cells in the subcutaneous MC38 tumor model.<sup>[37]</sup> Type-II interferon-γ (IFN-γ) significantly increased in the tumors after Hf-TBP/COD(+) treatment (Figure 5f; Figure S42a, Supporting Information), whereas pro-inflammatory cytokines including interleukin-6 (IL-6, Figure 5g; Figure S42b, Supporting Information) and tumor necrosis factor-α (TNF-α, Figure 5h; Figure S42c, Supporting Information) increased in both Hf-TBP(+) and Hf-TBP/COD(+) groups. While Hf-TBP-mediated PDT induced the secretion of IL-6 and TNF-α to elicit innate immune responses, Hf-TBP/COD(+) treatment synergized COD-catalyzed cholesterol depletion and PDT-induced ICD to secrete IFN-γ and triggered adaptive immune responses.<sup>[38]</sup> We then profiled the infiltration of DCs and cytotoxic T cells in the TME by flow cytometry. Hf-TBP/COD(+) treatment increased the percentage of MHCII<sup>+</sup>CD11c<sup>+</sup>DCs in CD11b<sup>+</sup> cells to 14.32% from 10.7% for PBS treatment (Figure 5i; Figures S43 and S44, Supporting Information), suggesting the potential of mediating downstream immune responses through the proliferation of T cells.<sup>[39]</sup> Flow cytometric analysis showed that Hf-TBP/COD(+)

treatment increased the infiltration of CD8<sup>+</sup> T cell percentage in tumors to 22.95% from 15.95% for PBS control (Figure 5j; Figure S45, Supporting Information). Immunofluorescence staining of tumor tissues supported the reinvigoration of T cells. More CD3<sup>+</sup> T cells were found in Hf-TBP/COD(+)-treated tumor tissues (Figure 5k), indicating the generation of a more T-cell-inflamed TME.

## 2.6. Antitumor Efficacy in 4T1 and MC38 Tumor Models

The in vivo antitumor efficacy of Hf-TBP/COD(+) was evaluated in subcutaneous 4T1-bearing BALB/c mice and MC38-bearing C57BL/6 mice (Figure 6a). Hf-TBP, COD, or Hf-TBP/COD was intratumorally injected at equivalent doses of 2.24 unit COD and 0.2 μmol of Hf-TBP (based on TBP), followed by irradiation with a 660 nm LED at 100 mW cm<sup>-2</sup> for 15 min (Figure 6a). Hf-TBP/COD treatment slightly slowed tumor growth with tumor growth inhibition (TGI) indices of 36.6% and 26.7% for 4T1 and MC38 tumors, respectively (Table S3, Supporting Information). Hf-TBP(+) moderately inhibited tumor growth with TGI values of 54.3% and 79.8% for 4T1 and MC38 tumors, respectively. In stark contrast, Hf-TBP/COD(+) effectively inhibited the growth of 4T1 and MC38 tumors with TGI values of 91.7% and 95.0%, respectively (Figure 6b–g; Figures S46 and S47, Supporting Information). 1 out of 5 mice with 4T1 tumors became tumor-free (Figure 6f). Sequential injection of COD and Hf-TBP followed by light irradiation gave a TGI of 64.8% for 4T1 tumors, which is significantly lower than the TGI value of 91.7% for Hf-TBP/COD(+). This result indicates the importance of loading COD in Hf-TBP to increase retention of COD in the tumors and facilitate COD uptake by cancer cells (Figure S48, Supporting Information). These results indicate excellent antitumor efficacy of Hf-TBP/COD(+) treatment due to the synergistic effects between Hf-TBP-mediated PDT and COD-catalyzed cholesterol depletion (Table S4, Supporting Information).

Hematoxylin and eosin (H&E) staining of tumor tissues further demonstrated obvious damages caused by Hf-TBP/COD(+) with severely altered tissue morphology and a decreased density of cell nuclei (Figure 6h).<sup>[40]</sup> Terminal deoxynucleotidyl transferase dUTP nick end labeling (TUNEL) staining revealed that Hf-TBP/COD(+) treatment caused more DNA fragmentation and ICD than Hf-TBP(+) treatment (Figure 6i), which might result from successful stimulation of caspase-1 mediated pyroptosis (Figure 6j). Importantly, H&E staining showed no abnormalities for major organs including heart, liver, spleen, lungs, and kidneys (Figure S49, Supporting Information). No significant body weight loss was observed for all treatment groups (Figure S50, Supporting Information). These results indicate that Hf-TBP/COD is a biocompatible nanoplatfor for synergistic cholesterol depletion and PDT to elicit potent antitumor effects.

d) TIM-3 in T cells of MC38 tumors after intratumoral injection of Hf-TBP/COD, COD, Hf-TBP (TBP = 0.2 μmol; and COD = 2.24 unit) followed by light irradiation (660 nm, 90 J cm<sup>-2</sup>) on day 14. e) Cholesterol levels in tumor tissues detected with Filipin III by flow cytometry (*n* = 5). Intratumoral concentrations of f) inflammatory cytokine IFN-γ, g) IL-6, and h) TNF-α detected by enzyme-linked immunosorbent assays (ELISA). i) Percentages of DCs (CD45<sup>+</sup> CD11b<sup>+</sup> MHCII<sup>+</sup> CD11c<sup>+</sup>) in myeloid cells (CD45<sup>+</sup> CD11b<sup>+</sup>) (*n* = 5). \*, *p* < 0.05; \*\*, *p* < 0.01; \*\*\*, *p* < 0.001; and \*\*\*\*, *p* < 0.0001. j) Percentages of cytotoxic T cells (CD8<sup>+</sup>) in total T cells (CD45<sup>+</sup> CD3<sup>+</sup>). k) CD3<sup>+</sup> T cells in 4T1 tumor tissues after different treatments; the scale bar: 50 μm.

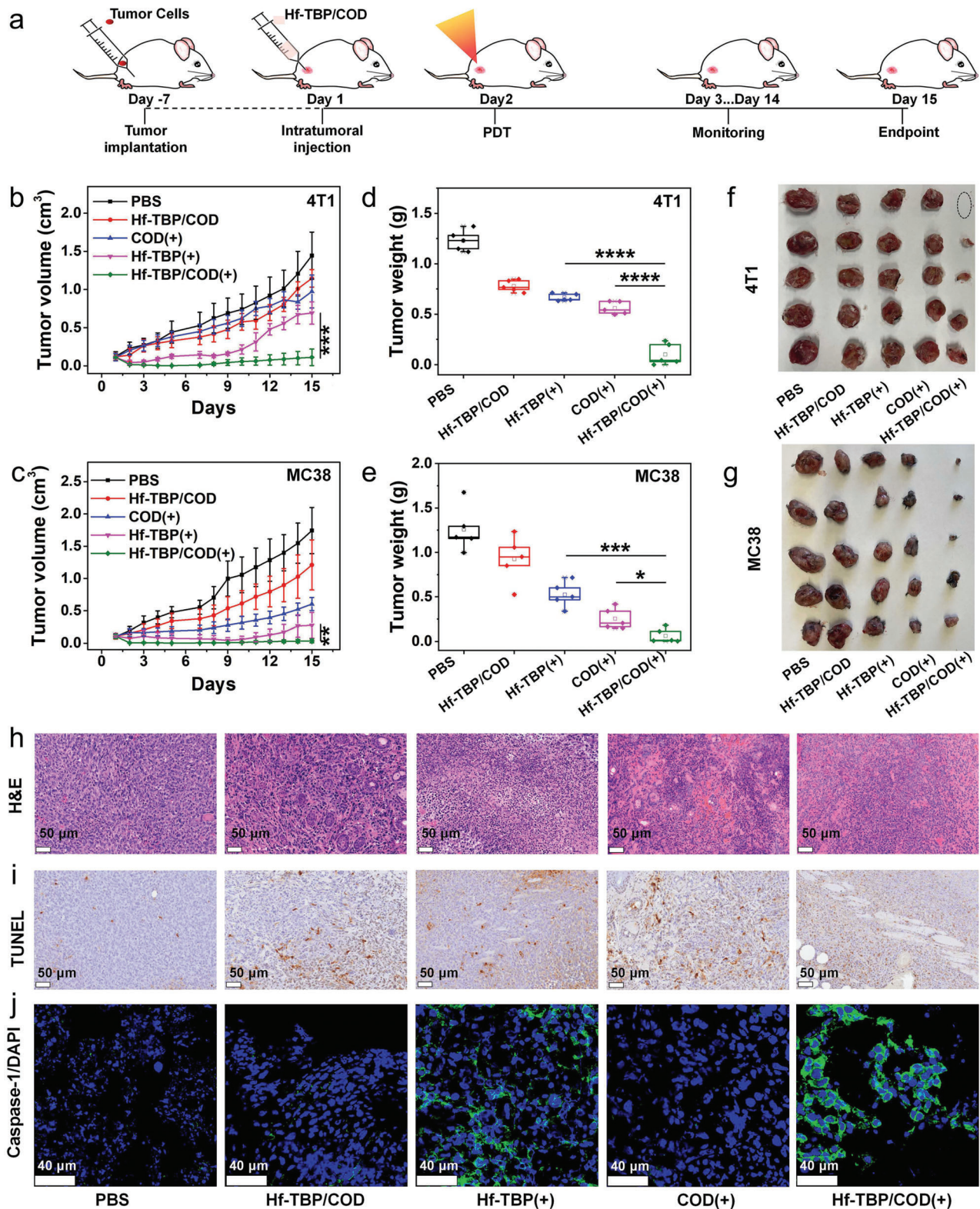


**Figure 6.** a) Treatment schema for tumor-bearing mice. b–e) Tumor volumes of 4T1 tumors (b) and MC38 tumors (c) and tumor weights of 4T1 tumors (d) and MC38 tumors (e) after different treatments ( $n = 5$ ). f, g) Photographs of excised 4T1 (f) and MC38 tumors (g) after different treatments. h) H&E staining of 4T1 tumor tissues after different treatments. i) Representative images of TUNEL staining of excised 4T1 tumors. ( $n = 5$ ; \*,  $p < 0.05$ ; \*\*,  $p < 0.01$ ; \*\*\*,  $p < 0.001$ ; and \*\*\*\*,  $p < 0.0001$ ), the scale bar: 50  $\mu\text{m}$ . j) Caspase-1 expression in the 4T1 tumor tissues after different treatments: the scale bar: 40  $\mu\text{m}$ .

### 3. Conclusion

We found that cholesterol depletion increased the membrane mechanical tension, osmotic fragility, rupturing propensity, and decreased the tolerance to oxidative stress of cancer cells. Based on these observations, we designed a Hf-TBP/COD nanoplatform to synergize cholesterol depletion and Hf-TBP-mediated PDT for enhanced antitumor effects. Hf-TBP/COD compromised the integrity of cancer cell membranes via extracting cholesterol from the phospholipid bilayer, generated ROS via the PDT process and COD-mediated biocatalysis, reduced the tolerance of cancer cells to ROS, and enhanced caspase-1-dependent pyroptosis. Hf-TBP/COD also remodeled the immuno-suppressive TME by targeting cholesterol metabolism through effective downregulation of immune checkpoints in the T cells, including PD-1, LAG-3, TIM-3, and 2B4 for improved T-cell activity. As an enzyme-functionalized nanophotosensitizer, Hf-TBP/COD simultaneously enhanced ICD of cancer cells and ameliorated the suppressive TME to afford potent antitumor efficacy in murine triple-negative breast cancer 4T1 and murine colon adenocarcinoma MC38 models. This work highlights the potential of MOFs as a versatile nanoplatform to enable novel strategies for effective cancer therapy.

### Supporting Information

Supporting Information is available from the Wiley Online Library or from the author.

### Acknowledgements

W.Z. and T.L. contributed equally to this work. This work was supported by the National Cancer Institute (1R01CA253655), the University of Chicago Medicine Comprehensive Cancer Center (NIH CCSG: P30 CA014599), and the Ludwig Institute for Metastasis Research for funding support. All animal experiments were conducted under protocol (ACUP72408), reviewed and approved by the Institutional Animal Care and Use Committee (IACUC) at the University of Chicago.

### Conflict of Interest

W.L. is the founder of Coordination Pharmaceuticals, which licensed the nMOF technology from the University of Chicago. R.R.W. is a consultant to Coordination Pharmaceuticals.

### Data Availability Statement

The data that support the findings of this study are available from the corresponding author upon reasonable request.

### Keywords

cholesterol depletion, immune checkpoints, nanoscale metal–organic frameworks, pyroptosis, tumor microenvironment remodeling

Received: June 29, 2023  
Revised: July 27, 2023  
Published online:

- [1] a) K. Lei, A. Kurum, M. Kaynak, L. Bonati, Y. Han, V. Cencen, M. Gao, Y. Q. Xie, Y. Guo, M. T. Hannebelle, Y. Wu, *Nat. Biomed. Eng.* **2021**, *5*, 1411; b) D. Roy, J. Steinkühler, Z. Zhao, R. Lipowsky, R. Dimova, *Nano Lett.* **2020**, *20*, 3185.
- [2] R. Sakamoto, D. S. Banerjee, V. Yadav, S. Chen, M. Gardel, C. Sykes, S. Banerjee, M. P. Murrell, *Commun. Biol.* **2023**, *6*, 325.
- [3] Y. Wang, Y. Liu, H. A. DeBerg, T. Nomura, M. T. Hoffman, P. R. Rohde, K. Schulten, B. Martinac, P. R. Selvin, *Elife* **2014**, *3*, e01834.
- [4] P. H. Wu, D. R. Aroush, A. Asnacios, W. C. Chen, M. E. Dokukin, B. L. Doss, P. Durand-Smet, A. Ekpenyong, J. Guck, N. V. Guz, P. A. Janmey, *Nat. Methods* **2018**, *15*, 491.
- [5] A. Colom, E. Derivery, S. Soleimanpour, C. Tomba, M. D. Molin, N. Sakai, M. González-Gaitán, S. Matile, A. Roux, *Nat. Chem.* **2018**, *10*, 1118.
- [6] a) A. J. Kosmalska, L. Casares, A. Elosegui-Artola, J. J. Thottacherry, R. Moreno-Vicente, V. González-Tarragó, M. Á. Del Pozo, S. Mayor, M. Arroyo, D. Navajas, X. Trepat, *Nat. Commun.* **2015**, *6*, 7292; b) B. Sinha, D. Köster, R. Ruez, P. Gonnord, M. Bastiani, D. Abankwa, R. V. Stan, G. Butler-Browne, B. Védie, L. Johannes, N. Morone, *Cell* **2011**, *144*, 402.
- [7] a) S. Parpal, M. Karlsson, P. Stralfors, *J. Biol. Chem.* **2001**, *276*, 9670; b) T. Richter, M. Floetenmeyer, R. G. Parton, *Traffic* **2008**, *9*, 893; c) C. J. Fielding, P. E. Fielding, *Biochim. Biophys. Acta.* **2000**, *1529*, 210.
- [8] a) F. R. Maxfield, I. Tabas, *Nature* **2005**, *438*, 612; b) T. Portet, R. Dimova, *Biophys. J.* **2010**, *99*, 3264.
- [9] a) J. L. Goldstein, M. S. Brown, *Nature* **1990**, *343*, 425; b) H. Buchwald, *Lancet* **1992**, *339*, 1154; c) J. Kopecka, M. Godel, C. Riganti, *Int. J. Biochem. Cell Biol.* **2020**, *129*, 105876; d) J. Yang, L. Wang, R. Jia, *J. Cancer* **2020**, *11*, 1761.
- [10] a) H. Halimi, S. Farjadian, *Front. Immunol.* **2022**, *13*, 7060; b) G. Lai, H. Liu, J. Deng, K. Li, C. Zhang, X. Zhong, B. Xie, *Cells* **2023**, *12*, 755.
- [11] a) E. J. Wherry, *Nat. Immunol.* **2011**, *12*, 492; b) X. Ma, E. Bi, Y. Lu, P. Su, C. Huang, L. Liu, Q. Wang, M. Yang, M. F. Kalady, J. Qian, A. Zhang, A. A. Gupte, D. J. Hamilton, C. Zheng, Q. Yi, *Cell Metab.* **2019**, *30*, 143; c) D. B. Johnson, C. A. Nebhan, J. J. Moslehi, J. M. Balko, *Nat. Rev. Clin. Oncol.* **2022**, *19*, 254; d) J. Ni, Z. Zhang, M. Ge, J. Chen, W. Zhuo, *Acta Pharmacol. Sin.* **2023**, *44*, 288; e) I. Giacomini, F. Gianfanti, M. A. Desbats, G. Orso, M. Berretta, T. Prayer-Galetti, E. Ragazzi, V. Cocetta, *Front. Oncol.* **2021**, *11*, 682911; f) B. Huang, B. L. Song, C. Xu, *Nat. Metab.* **2020**, *2*, 132.
- [12] Z. Zheng, Z. Jia, C. Qu, R. Dai, Y. Qin, S. Rong, Y. Liu, Z. Cheng, R. Zhang, *Small* **2021**, *17*, 2006508.
- [13] a) Y. Zou, D. Kim, M. Yagi, Y. Yamasaki, J. Kurita, T. Iida, Y. Matsuyama, K. Yamaguchi, T. Oda, *Biosci. Biotechnol. Biochem.* **2013**, *77*, 345; b) M. A. Davis, M. R. Fairgrieve, A. Den Hartigh, O. Yakovenko, B. Duvvuri, C. Lood, W. E. Thomas, S. L. Fink, M. Gale, *Proc. Natl. Acad. Sci. USA* **2019**, *116*, 5061.
- [14] A. Claude-Taupin, J. Jia, Z. Bhujabal, M. Garfa-Traoré, S. Kumar, G. P. D. da Silva, R. Javed, Y. Gu, L. Allers, R. Peters, F. Wang, *Nat. Cell Biol.* **2021**, *23*, 846.
- [15] B. Pontes, P. Monzo, L. Gole, A. L. Le Roux, A. J. Kosmalska, Z. Y. Tam, W. Luo, S. Kan, V. Viasnoff, P. Roca-Cusachs, L. Tucker-Kellogg, *J. Cell Biol.* **2017**, *216*, 2959.
- [16] a) N. C. Gauthier, M. A. Fardin, P. Roca-Cusachs, M. P. Sheetz, *Proc. Natl. Acad. Sci. USA* **2011**, *108*, 14467; b) K. Keren, Z. Pincus, G. M. Allen, E. L. Barnhart, G. Marriott, A. Mogilner, J. A. Theriot, *Nature* **2008**, *453*, 475.
- [17] a) L. Cheng, C. Wang, L. Feng, K. Yang, Z. Liu, *Chem. Rev.* **2014**, *114*, 10869; b) J. Ouyang, A. Xie, J. Zhou, R. Liu, L. Wang, H. Liu, N. Kong, W. Tao, *Chem. Soc. Rev.* **2022**, *51*, 4996; c) Y. Jiang, J. Li, Z. Zeng, C. Xie, Y. Lyu, K. Pu, *Angew. Chem., Int. Ed.* **2019**, *58*, 8161; d) Y. Liu, Y. Wang, S. S., H. Zhang, *Natl. Sci. Rev.* **2022**, *9*, 139; e) M. Overchuk, R. A. Weersink, B. C. Wilson, G. Zheng, *ACS Nano* **2023**, *17*, 7979.

- [18] a) B. Chen, Y. Yan, Y. Yang, G. Cao, X. Wang, Y. Wang, F. Wan, Q. Yin, Z. Wang, Y. Li, L. Wang, B. Xu, F. You, Q. Zhang, Y. Wang, *Nat. Nanotechnol.* **2022**, *17*, 788; b) J. Zhou, X. Ma, H. Li, D. Chen, L. Mao, L. Yang, T. Zhang, W. Qiu, Z. Xu, Z. J. Sun, *Nano Res.* **2022**, *15*, 3398; c) M. Li, Y. Xu, X. Peng, J. S. Kim, *Acc. Chem. Res.* **2022**, *55*, 3253.
- [19] a) Y. Song, L. Wang, Z. Xie, *Biotechnol. J.* **2021**, *16*, 1900382; b) G. Lan, K. Ni, W. Lin, *Coord. Chem. Rev.* **2019**, *379*, 65; c) Z. Xu, T. Luo, W. Lin, *Acc. Mater. Res.* **2021**, *2*, 944; d) Y. Li, L. Wang, H. Liu, Y. Pan, C. Li, Z. Xie, X. Jing, *Small* **2021**, *17*, 2100756; e) M. Lismont, L. Dreesen, S. Wuttke, *Adv. Funct. Mater.* **2017**, *27*, 1606314; f) L. Dai, M. Yao, Z. Fu, X. Li, X. Zheng, S. Meng, Z. Yuan, K. Cai, H. Yang, Y. L. Zhao, *Nat. Commun.* **2022**, *13*, 2688; g) D. Wang, I. W. He, J. Liu, D. Jana, Y. Wu, X. Zhang, C. Qian, Y. Guo, X. Chen, A. K. Bindra, Y. L. Zhao, *Angew. Chem., Int. Ed.* **2021**, *60*, 26254; h) R. Ettlenger, U. Lächelt, R. Gref, P. Horcajada, T. Lammers, C. Serre, P. Couvreur, R. E. Morris, S. Wuttke, *Chem. Soc. Rev.* **2022**, *51*, 464; i) S. Wang, S. S. Park, C. T. Buru, H. Lin, P. C. Chen, E. W. Roth, O. K. Farha, C. A. Mirkin, *Nat. Commun.* **2020**, *11*, 2495.
- [20] a) Z. Wang, Y. Fu, Z. Kang, X. Liu, N. Chen, Q. Wang, Y. Tu, L. Wang, S. Song, D. Ling, H. Song, X. Kong, C. Fan, *J. Am. Chem. Soc.* **2017**, *139*, 15784; b) J. Y. Oh, E. Choi, B. Jana, E. M. Go, E. Jin, S. Jin, J. Lee, J. H. Bae, G. Yang, S. K. Kwak, W. Choe, *Small* **2023**, *19*, 2300218; c) X. Wu, H. Yue, Y. Zhang, X. Gao, X. Li, L. Wang, Y. Cao, M. Hou, H. An, L. Zhang, S. Li, *Nat. Commun.* **2019**, *10*, 5165.
- [21] a) K. Lu, C. He, N. Guo, C. Chan, K. Ni, R. R. Weichselbaum, W. Lin, *J. Am. Chem. Soc.* **2016**, *138*, 12502; b) G. Lan, K. Ni, Z. Xu, S. S. Veroneau, Y. Song, Lin, W., *J. Am. Chem. Soc.* **2018**, *140*, 5670; c) K. Lu, C. He, N. Guo, C. Chan, K. Ni, G. Lan, H. Tang, C. Pelizzari, Y. X. Fu, M. T. Spiotto, R. R. Weichselbaum, W. Lin, *Nat. Biomed. Eng.* **2018**, *2*, 6000.
- [22] D. Feng, Z. Y. Gu, J. R. Li, H. L. Jiang, Z. Wei, H. C. Zhou, *Angew. Chem., Int. Ed.* **2012**, *51*, 10307.
- [23] Y. Wang, J. Yan, N. Wen, H. Xiong, S. Cai, Q. He, Y. Hu, D. Peng, Z. Liu, Y. Liu, *Biomaterials* **2020**, *230*, 119619.
- [24] a) W. Zhen, Y. Liu, W. Wang, M. Zhang, W. Hu, X. Jia, C. Wang, X. Jiang, *Angew. Chem., Int. Ed.* **2020**, *59*, 9491; b) R. A. Silva, A. M. Carmona Ribeiro, D. F. Petri, *Colloids Surf., B* **2013**, *110*, 347.
- [25] T. Luo, G. T. Nash, Z. Xu, X. Jiang, J. Liu, W. Lin, *J. Am. Chem. Soc.* **2021**, *143*, 135194.
- [26] a) S. Boulant, C. Kural, J. C. Zeeh, F. Ubelmann, T. Kirchhausen, *Nat. Cell Biol.* **2011**, *13*, 1124; b) M. Saleem, S. Morlot, A. Hohendahl, J. Manzi, M. Lenz, A. Roux, *Nat. Commun.* **2015**, *6*, 6249.
- [27] a) M. Ding, Y. Zhang, J. Li, K. Pu, *Nano Convergence* **2022**, *9*, 7; b) N. Yin, Y. Wang, Y. Huang, Y. Cao, L. Jin, J. Liu, T. Zhang, S. Song, X. Liu, H. Zhang, *Adv. Sci.* **2023**, *10*, 2204937; c) S. Dong, Y. Dong, B. Liu, J. Liu, S. Liu, Z. Zhao, W. Li, B. Tian, R. Zhao, F. He, S. Gai, *Adv. Mater.* **2022**, *34*, 2107054.
- [28] C. Gabella, E. Bertseva, C. Bottier, N. Piacentini, A. Bornert, S. Jeney, L. Forró, I. F. Szbalzarini, J. J. Meister, A. B. Verkhovskiy, *Curr. Biol.* **2014**, *24*, 1126.
- [29] a) Y. Xiao, T. Zhang, X. Ma, Q. C. Yang, L. L. Yang, S. C. Yang, M. Liang, Z. Xu, Z. J. Sun, *Adv. Sci.* **2021**, *8*, 2101840; b) Y. Liu, W. Zhen, Y. Wang, S. Song, H. Zhang, *J. Am. Chem. Soc.* **2020**, *142*, 21751; c) W. Zhen, Y. Liu, S. An, X. Jiang, *Angew. Chem., Int. Ed.* **2023**, *135*, 202301866.
- [30] a) W. Zhen, S. An, S. Wang, W. Hu, Y. Li, X. Jiang, J. Li, *Adv. Mater.* **2021**, *33*, 2101572; b) W. Zhen, R. R. Weichselbaum, W. Lin, *Adv. Mater.* **2023**, *35*, 2206370; c) P. Broz, P. Pelegrín, F. Shao, *Nat. Rev. Immunol.* **2020**, *20*, 143; d) Q. Wang, Y. Wang, J. Ding, C. Wang, X. Zhou, W. Gao, H. Huang, F. Shao, Z. Liu, *Nature* **2020**, *579*, 421.
- [31] a) W. Jiang, L. Yin, H. Chen, A. V. Paschall, L. Zhang, W. Fu, W. Zhang, T. Todd, K. S. Yu, S. Zhou, Z. Zhen, M. Butler, L. Yao, F. Zhang, Y. Shen, Z. Li, A. Yin, H. Yin, X. Wang, F. Y. Avci, X. Yu, J. Xie, *Adv. Mater.* **2019**, *31*, 1904058; b) F. Shao, *Nat. Rev. Immunol.* **2021**, *21*, 620. c) G. Jody, L. Jeffrey, M. Marek, *Mol. Cells* **2004**, *17*, 383; d) M. P. Chao, S. Jaiswal, R. Weissman Tsukamoto, A. A. Alizadeh, A. J. Gentles, J. Volkmer, K. Weiskopf, S. B. Willingham, T. Raveh, C. Y. Park, R. Majeti, I. L. Weissman, *Sci. Transl. Med.* **2010**, *2*, 63ra94; e) D. V. Krysko, K. S. Ravichandran, P. Vandenabeele, *Nat. Commun.* **2018**, *9*, 4644.
- [32] a) A. Del Prete, V. Salvi, A. Soriani, M. Laffranchi, F. Sozio, D. Bosisio, S. Sozzani, *Cell. Mol. Immunol.* **2023**, *20*, 432; b) Y. J. Liu, H. Kanzler, V. Soumelis, M. Gilliet, *Nat. Immunol.* **2001**, *2*, 585; c) M. L. Kapsenberg, *Nat. Rev. Immunol.* **2003**, *3*, 984.
- [33] Z. Zeng, K. Pu, *Adv. Funct. Mater.* **2020**, *30*, 2004397.
- [34] D. V. Krysko, A. D. Garg, A. Kaczmarek, O. Krysko, P. Agostinis, P. Vandenabeele, *Nat. Rev. Cancer* **2012**, *12*, 860.
- [35] a) R. H. Deng, M. Z. Zou, D. Zheng, S. Y. Peng, W. Liu, X. F. Bai, H. S. Chen, Y. Sun, P. H. Zhou, X. Z. Zhang, *ACS Nano* **2019**, *13*, 8618; b) P. Liu, Y. Wang, L. An, Q. Tian, J. Lin, S. Yang, *ACS Appl. Mater. Interfaces* **2018**, *10*, 38833.
- [36] G. M. Cramer, E. K. Moon, K. A. Cengel, T. M. Busch, *Photochem. Photobiol.* **2020**, *96*, 954.
- [37] J. Lou, M. Aragaki, N. Bernards, T. Chee, A. Gregor, Y. Hiraishi, T. Ishiwata, C. Leung, L. Ding, S. Kitazawa, T. Koga, *Biomaterials* **2023**, *292*, 121918.
- [38] a) A. M. Gocher, C. J. Workman, D. A. A. Vignali, *Nat. Rev. Immunol.* **2022**, *22*, 158; b) G. P. Dunn, C. M. Koebel, R. D. Schreiber, *Nat. Rev. Immunol.* **2006**, *6*, 836; c) L. B. Ivashkiv, *Nat. Rev. Immunol.* **2018**, *18*, 545.
- [39] D. S. Chen, I. Mellman, *Nature* **2017**, *541*, 321.
- [40] D. S. Gareau, *J. Biomed. Opt.* **2009**, *14*, 034050.